Supporting Information

Engineering microporous ethane-trapping metal−organic frameworks for boosting ethane/ethylene separation

Jiyan Pei[a], Jia-Xin Wang[a], Kai Shao[a], Yu Yang[a], Yuanjing Cui[a], Hui Wu[b], Wei Zhou*[b], Bin Li*[a], and Guodong Qian*[a]

[a] State Key Laboratory of Silicon Materials, Cyrus Tang Center for Sensor Materials and Applications, Department of Materials Science & Engineering, Zhejiang University, Hangzhou 310027, China. E-mail: bin.li@zju.edu.cn; gdqian@zju.edu.cn

[b] NIST Center for Neutron Research, National Institute of Standards and Technology, Gaithersburg, MD 20899-6102, United States. E-mail: wzhou@nist.gov

1. General Procedures and Materials.

All starting reagents and solvents were purchased from commercial companies and used without further purification. Among them, nickel(II) chloride hexahydrate ($NiCl_2 \cdot 6H_2O$, CAS: 7791-20-0, 98%) was purchased from Energy Chemical, 1,4-diazabicyclo [2.2.2] octane (ted, CAS: 280-57-9, 98%) was purchased from Tokyo Chemical Industry, 1,4-naphthalenedicarboxylic acid (H_2ndc, CAS: 605-70-9, 98%) was purchased from Alfa Aesar, 9,10-anthracenedicarboxylic acid (H_2adc, CAS: 73016-08-7, 95%) was purchased from Sigma-Aldrich. Thermogravimetric analyses (TGA) were examined by using a Netzsch TG209F3 under N_2 atmosphere with a heating rate of 5 K min^{-1}. Powder X–ray diffraction (PXRD) patterns were collected in the 2θ = 2-45° range on an X'Pert PRO diffractometer with Cu Kα (λ = 1.542 Å) radiation at room temperature.

2. Powder X-ray Crystallography.

Attempts to obtain single crystals of ZJU-121 for single-crystal X-ray diffraction measurement were not successful. We thus relied on powder X-ray diffraction (PXRD) to confirm the high purity of the powder sample and to simulate the crystallographic structure. The PXRD measurements were performed on a Rigaku Ultima IV diffractometer, operated at 40 kV and 44 mA and CuKα radiation (λ = 1.5406 Å). Data were collected at room temperature in the 2θ range of 2-45° with a step size of 1.0°. We first indexed the PXRD pattern and used a triclinic *P1* space group to build the model of ZJU-121. Here we chose the low *P1* setting in order to build an ordered structure in a less oblique unit cell and to show the channel pore structure more clearly. Then, based on the framework connection of ZJU-120, we built a crystal structure model for ZJU-121. The anthracene groups were modeled as fully ordered in the structure and the orientation of anthracene rings was optimized. In reality, there might exist some orientational disorder associated with the anthracene groups. As shown in Fig. S3, the simulated PXRD pattern of our structural model agrees excellently with the experimental data, strongly supporting its validity.

3. Fitting of pure component isotherms.

The experimentally measured loadings for C_2H_6 and C_2H_4 measured at temperatures of 273 K and 296 K in ZJU-120a, $Ni(bdc)(ted)_{0.5}$ and ZJU-121a were fitted with the dual-Langmuir-Freundlich isotherm model

$$q = q_{A,sat}\frac{b_A p^{\nu_A}}{1+b_A p^{\nu_A}} + q_{B,sat}\frac{b_B p^{\nu_B}}{1+b_B p^{\nu_B}}$$

(1)

with T-dependent parameters b_A, and b_B

$$b_A = b_{A0}\exp\left(\frac{E_A}{RT}\right);\quad b_B = b_{B0}\exp\left(\frac{E_B}{RT}\right) \tag{2}$$

The parameters are provided in Table S2, S3 and S4.

4. Virial Graph Analysis.

Estimation of the isosteric heats of gas adsorption (Q_{st})

A virial-type expression of comprising the temperature-independent parameters a_i and b_j was employed to calculate the enthalpies of adsorption for C_2H_6 and C_2H_4 (at 273 K and 296 K) on ZJU-120a, Ni(bdc)(ted)$_{0.5}$ and ZJU-121a. In each case, the data were fitted use equation:

$$\ln P = \ln N + 1/T\sum_{i=0}^{m} a_i N_i + \sum_{j=0}^{n} b_j N_j \tag{3}$$

Here, P is the pressure expressed in mmHg, N is the amount absorbed in mmol g^{-1}, T is the temperature in K, a_i and b_j are virial coefficients, and m, n represent the number of coefficients required to adequately describe the isotherms (m and n were gradually increased till the contribution of extra added a and b coefficients was deemed to be statistically insignificant towards the overall fit. And the average value of the squared deviations from the experimental values was minimized). The values of the virial coefficients a_0 through a_m were then used to calculate the isosteric heat of absorption using the following expression:

$$Q_{st} = -R\sum_{i=0}^{m} a_i N_i \tag{4}$$

Q_{st} is the coverage-dependent isosteric heat of adsorption and R is the universal gas constant. The heat enthalpy of C_2H_6 and C_2H_4 sorption for complex ZJU-120a, Ni(bdc)(ted)$_{0.5}$ and ZJU-121a in this manuscript are determined by using the sorption data measured in the pressure range from 0-1 bar (at 273 K and 296 K).

5. IAST calculations.

The adsorption selectivity is defined by

$$S_{ads} = \frac{q_1/q_2}{p_1/p_2} \tag{5}$$

In equation (5), q_1 and q_2 are the molar loadings in the adsorbed phase in equilibrium with the bulk gas phase with partial pressures p_1, and p_2.

Notation

b_A	Langmuir-Freundlich constant for species *i* at adsorption site A, $Pa^{-\nu_{iA}}$
b_B	Langmuir-Freundlich constant for species *i* at adsorption site B, $Pa^{-\nu_{iB}}$
c_i	molar concentration of species *i* in gas mixture, mol m^{-3}
c_{i0}	molar concentration of species *i* in gas mixture at inlet to adsorber, mol m^{-3}
E	energy parameter, J mol^{-1}
p_i	partial pressure of species *i* in mixture, Pa
p_t	total system pressure, Pa
q_i	component molar loading of species *i*, mol kg^{-1}
Q_{st}	isosteric heat of adsorption, J mol^{-1}
T	absolute temperature, K

Greek letters

ν□	Freundlich exponent, dimensionless
ρ□	framework density, kg m^{-3}

Subscripts

i	referring to component *i*
t	referring to total mixture

Table S1. Lattice parameters of the crystal structure of ZJU-120.

Unit cell parameters	ZJU-120
Formula	$C_{15}H_{12}NNiO_4$
Formula weight	328.97
Crystal system	tetragonal
Space group	P4/mmm
a, *b* (Å)	10.8865(8)
c (Å)	9.3470(8)
α (°)	90.00
β (°)	90.00
γ (°)	90.00
V (Å^3)	1107.78(18)
Z	2
D_{calcd} (g cm^{-3})	0.986
CCDC	1953742

Table S2. Dual-Langmuir-Freundlich parameter fits for C_2H_6 and C_2H_4 in ZJU-120a. The fits are based on experimental isotherm data at 296 K.

	Site A			Site B		
	$q_{A,sat}$	b_{A0}	ν_A	$q_{B,sat}$	b_{B0}	ν_B
	mol kg^{-1}	k$Pa^{-\nu A}$	dimensionless	mol kg^{-1}	k$Pa^{-\nu B}$	dimensionless
C_2H_6	5.87938	0.07139	0.92421	0.40678	5.92081×10^{-5}	3.03253
C_2H_4	3.32789	0.04805	1.02858	1.38086	0.00213	1.65896

Table S3. Dual-Langmuir-Freundlich parameter fits for C_2H_6 and C_2H_4 in Ni(bdc)(ted)$_{0.5}$. The fits are based on experimental isotherm data at 296 K.

	Site A			Site B		
	$q_{A,sat}$	b_{A0}	ν_A	$q_{B,sat}$	b_{B0}	ν_B
	mol kg^{-1}	k$Pa^{-\nu A}$	dimensionless	mol kg^{-1}	k$Pa^{-\nu B}$	dimensionless
C_2H_6	1.10205	0.03557	1.11979	6.66668	3.61249×10^{-4}	1.83576
C_2H_4	2.6595	0.01054	1.04208	3.62703	1.27952×10^{-4}	1.90462

Table S4. Dual-Langmuir-Freundlich parameter fits for C_2H_6 and C_2H_4 in ZJU-121a. The fits are based on experimental isotherm data at 296 K.

	Site A			Site B		
	$q_{A,sat}$ mol kg^{-1}	b_{A0} $_kPa^{-\nu A}$	ν_A dimensionless	$q_{B,sat}$ mol kg^{-1}	b_{B0} $_kPa^{-\nu B}$	ν_B dimensionless
C_2H_6	2.45615	0.81988	1.05855	3.06365	0.00481	0.88053
C_2H_4	2.19951	0.41281	1.07426	11.32815	0.00909	0.52004

Table S5. Comparison of the C_2H_6 adsorption capacity and C_2H_6/C_2H_4 selectivity of ZJU-120a with other best-performing materials at room temperature.

	C_2H_6 adsorption uptake[a]		C_2H_4 adsorption uptake[a]	C_2H_6/C_2H_4 selectivity[b]	C_2H_6 Q_{st}[d] (kJ mol^{-1})	T (K)	Ref.
	0.5 bar (mmol g^{-1})	1.0 bar (mmol g^{-1})	1.0 bar (mmol g^{-1})				
ZJU-120a	4.29	4.91	3.93	2.74	27.6	296	This work
ZJU-121a	2.81	3.1	3.19	1.51	47.1	296	This work
Ni(bdc)(ted)$_{0.5}$	2.95	5.13	3.4	1.8	21.1	298	1
$Fe_2(O_2)$(dobdc)	3.04	3.29	2.54	4.4	66.8	298	2
Cu(Qc)$_2$	1.3	1.85	0.78	3.45	30	298	3
MAF-49	1.7	1.71	1.7	2.7	61	298	4
UiO-66-2CF$_3$	0.6	0.88	0.5	2.54	14.5	298	5
ZIF-4	2.23	2.3	2.2	2.15	-	293	6
Ni(TMBDC)(DABCO)$_{0.5}$	5	5.44	5	1.98[c]	39.6	298	7
MUF-15	3.92	4.67	4.17	1.96	29.2	293	8
ZIF-8	1.43	2.54	1.43	1.8	17.2	293	9
PCN-245	1.94	3.31	2.4	1.8	22.8	298	10
IRMOF-8	2.5	4.2	2.8	1.7	52.5	298	11
MIL-142A	2.29	3.84	2.9	1.51	27.2	298	12
ZIF-7	1.82	2	1.9	1.5	-	298	13
MIL-53(Al)	1.53	2.05	1.69	1.3	22.2	323	14

[a] Adsorption uptake obtained from single-component gas adsorption isotherms

[b] Selectivity is calculated by IAST for an equimolar mixture at 1 bar

[c] Selectivity is for a 1/15 mixture

[d] Q_{st} values at zero coverage

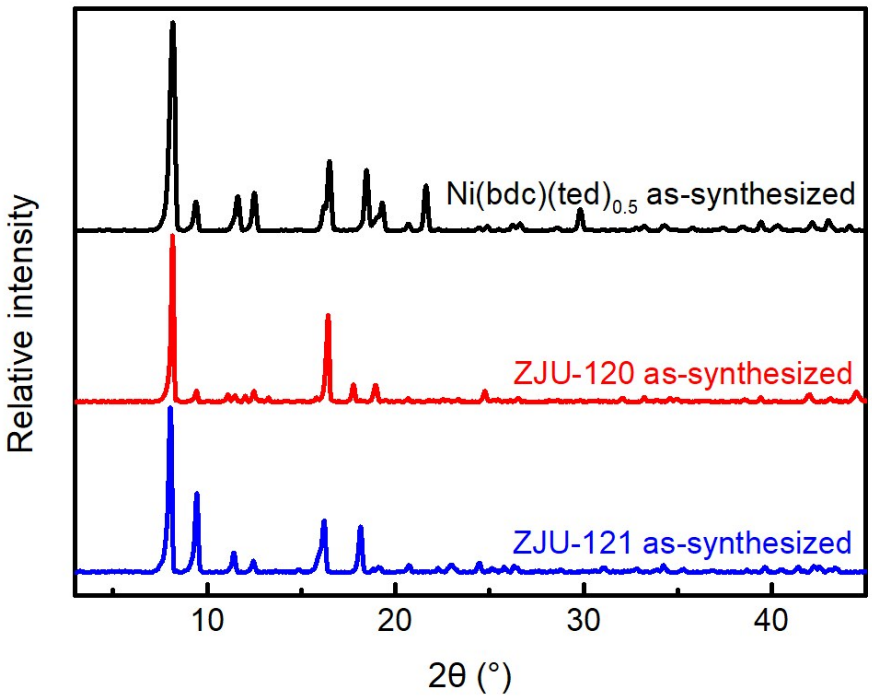

Figure S1. Experimental PXRD patterns of as-synthesized $Ni(bdc)(ted)_{0.5}$ (black), ZJU-120 (red) and ZJU-121 (blue), all of which match well with each other.

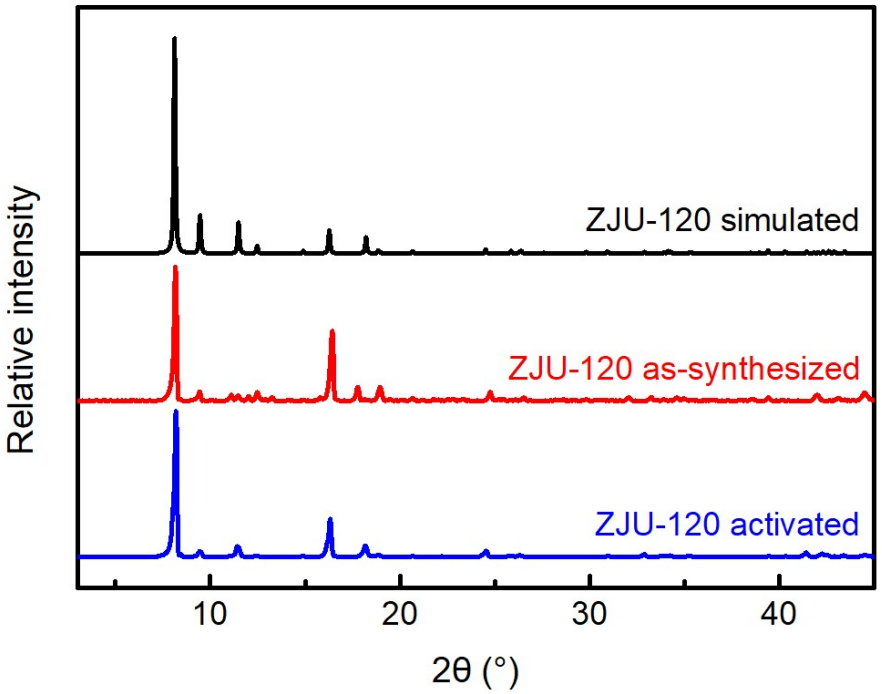

Figure S2. The simulated XRD pattern from the crystal of ZJU-120 (black) and PXRD patterns of as-synthesized ZJU-120 (red), activated ZJU-120 (blue).

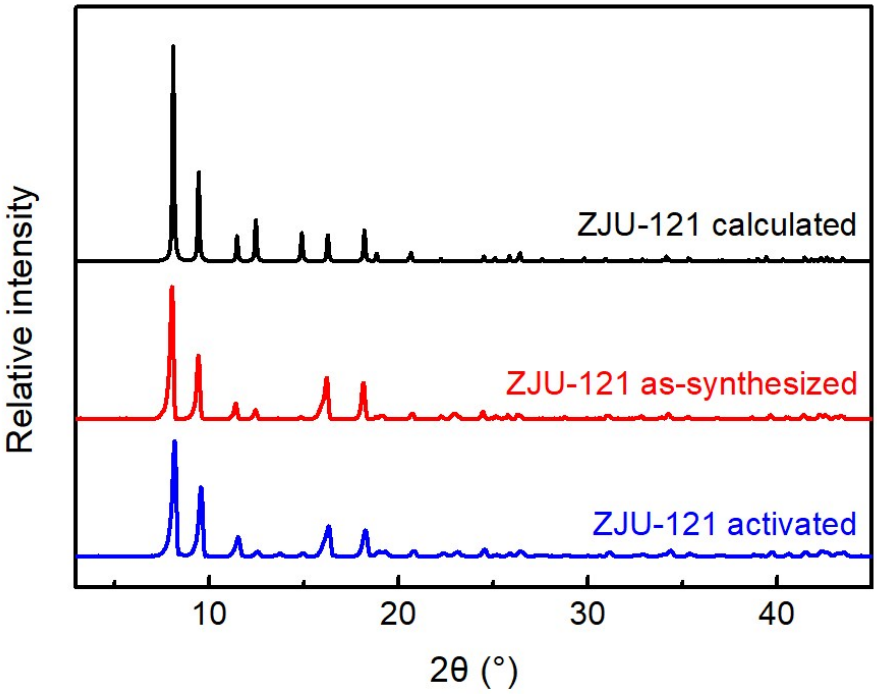

Figure S3. The calculated XRD pattern from the model structure of ZJU-121 (black) and PXRD patterns of as-synthesized ZJU-121 (red), activated ZJU-121 (blue). The simulated PXRD pattern of our structural model agrees excellently with the experimental data, strongly supporting its validity.

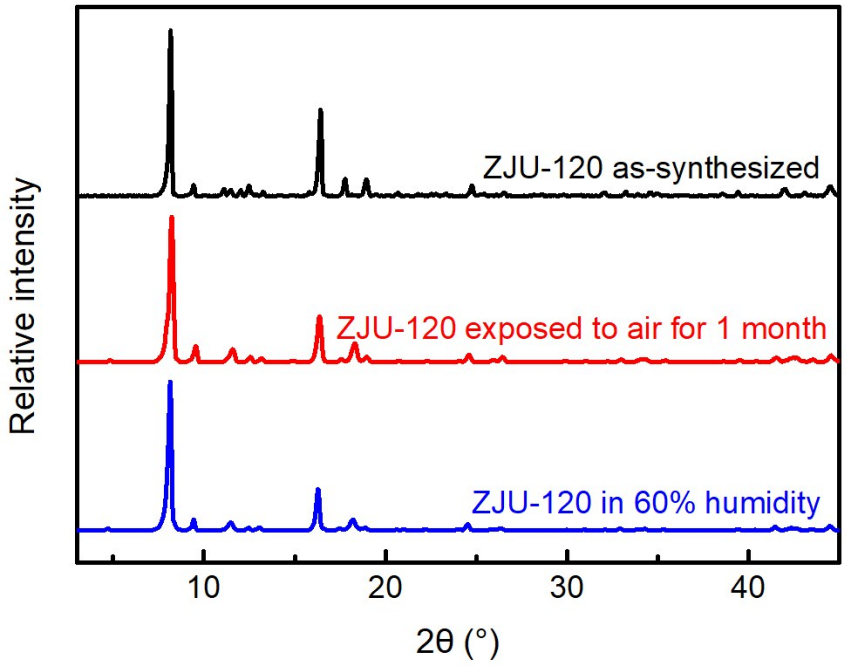

Figure S4. PXRD patterns of as-synthesized ZJU-120 (black), the sample exposed to air for 1 month (red) and exposed to 60% humidity (blue), indicating its good stability.

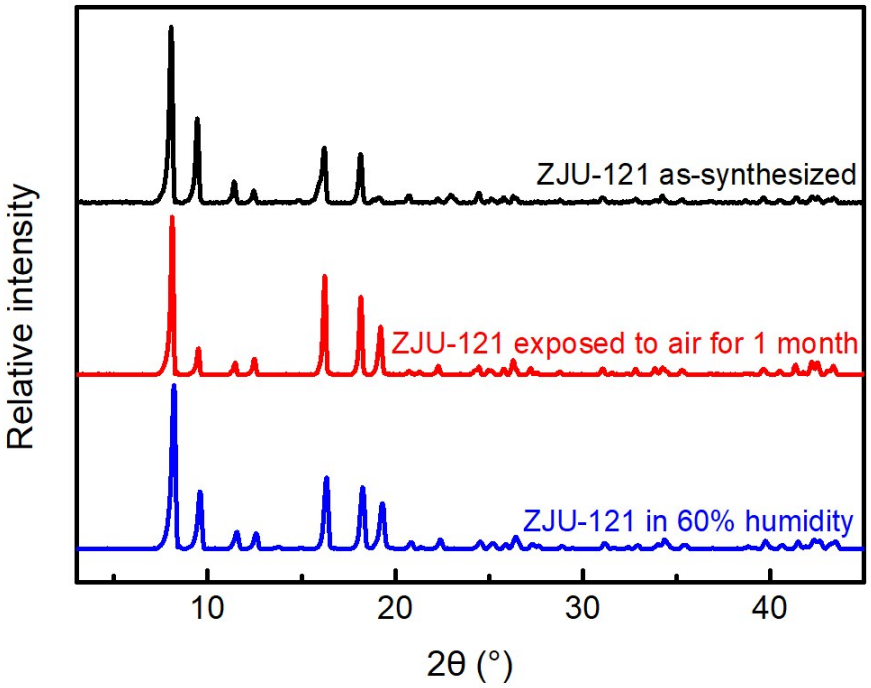

Figure S5. PXRD patterns of as-synthesized ZJU-121 (black), the sample exposed to air for 1 month (red) and exposed to 60% humidity (blue), indicating its good stability.

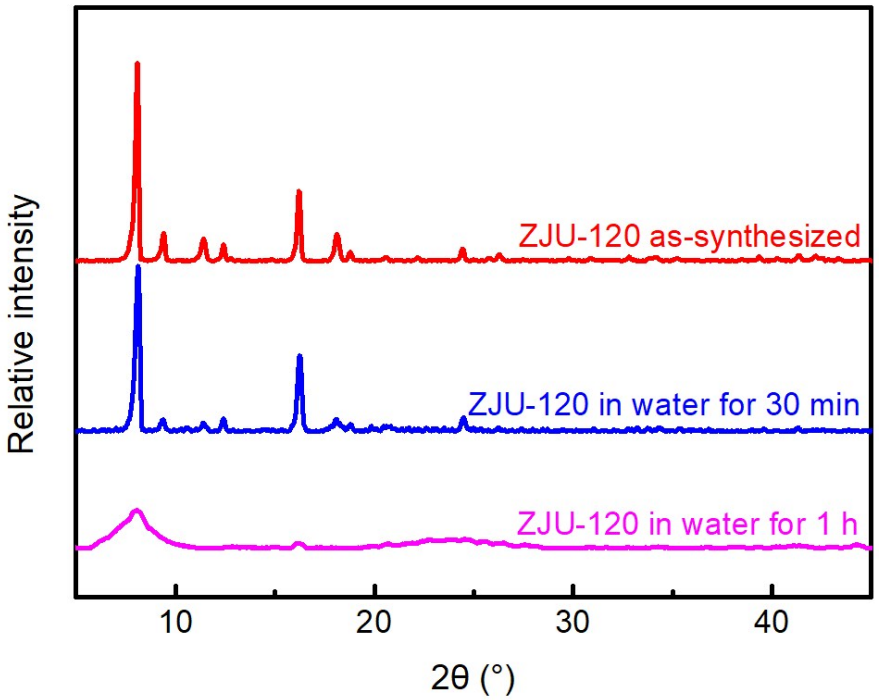

Figure S6. PXRD patterns of as-synthesized ZJU-120 (red), the sample in water for 30 min (blue) and 1 h (pink), indicating its certain water stability.

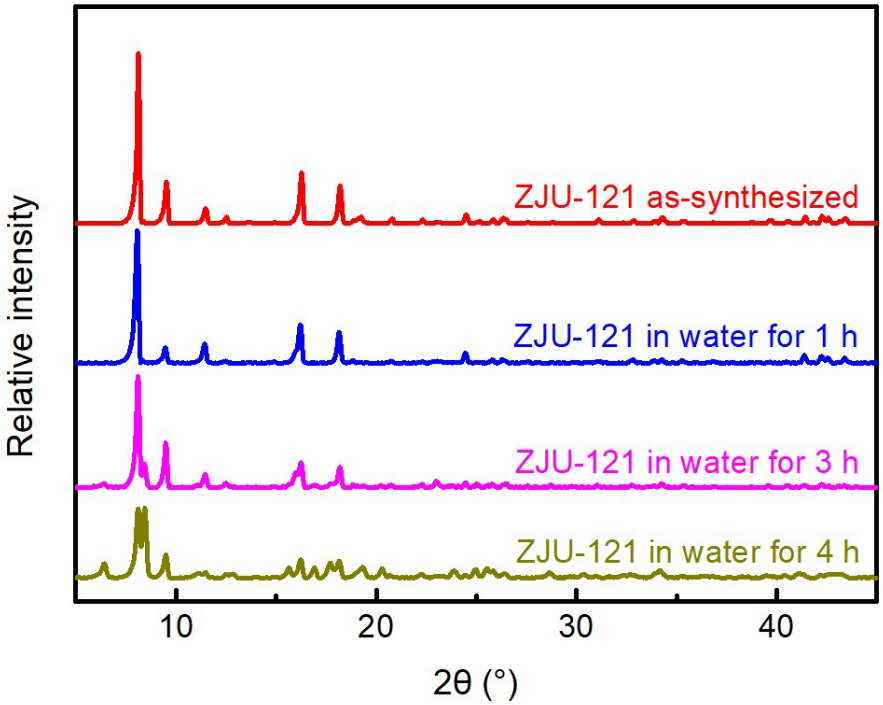

Figure S7. PXRD patterns of as-synthesized ZJU-121 (red), the sample in water for 1 h (blue), 3 h (pink) and 4 h (yellow), indicating its certain water stability.

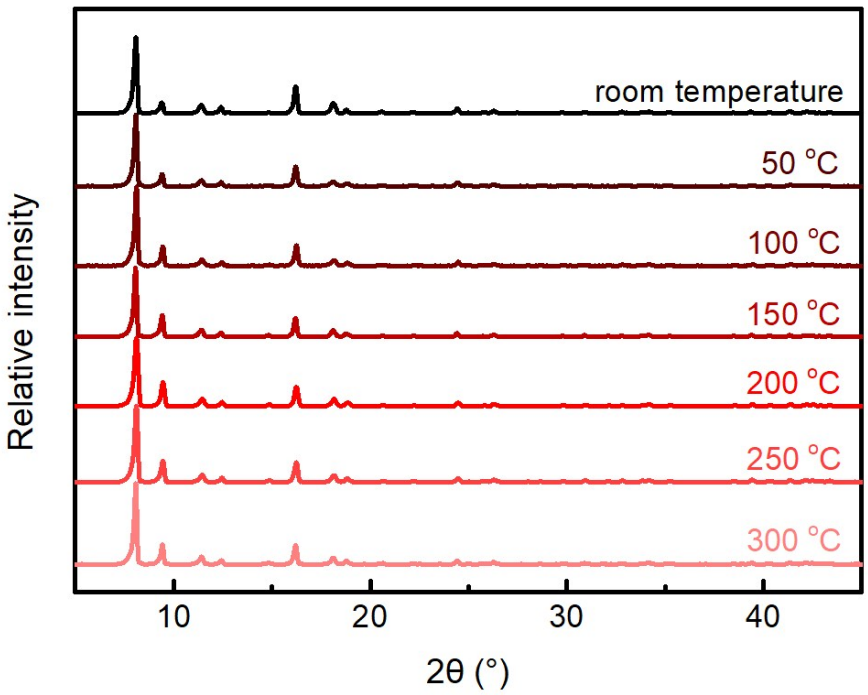

Figure S8. Variable-temperature PXRD patterns for ZJU-120.

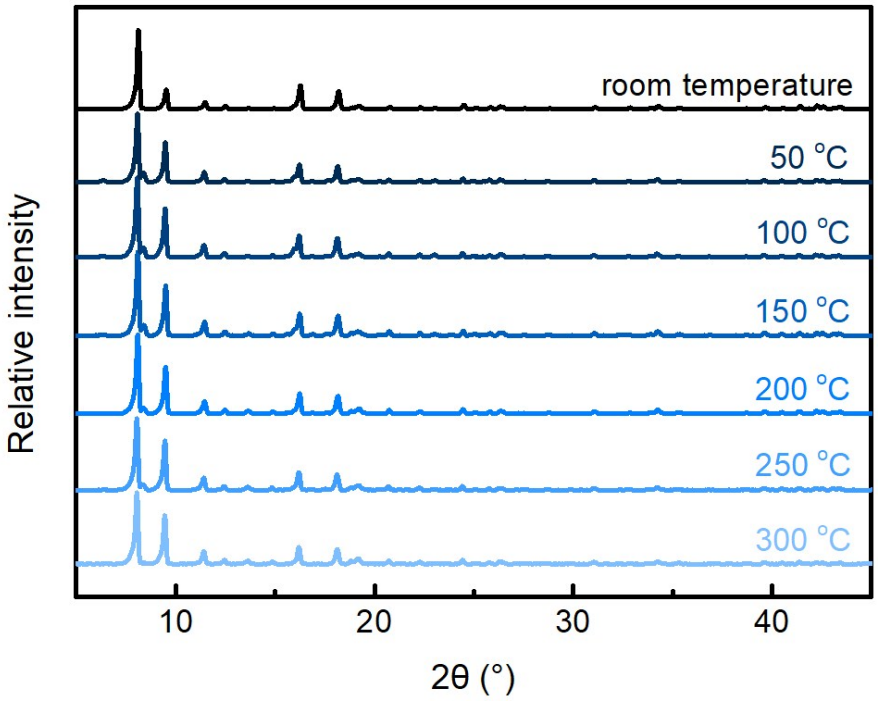

Figure S9. Variable-temperature PXRD patterns for ZJU-121.

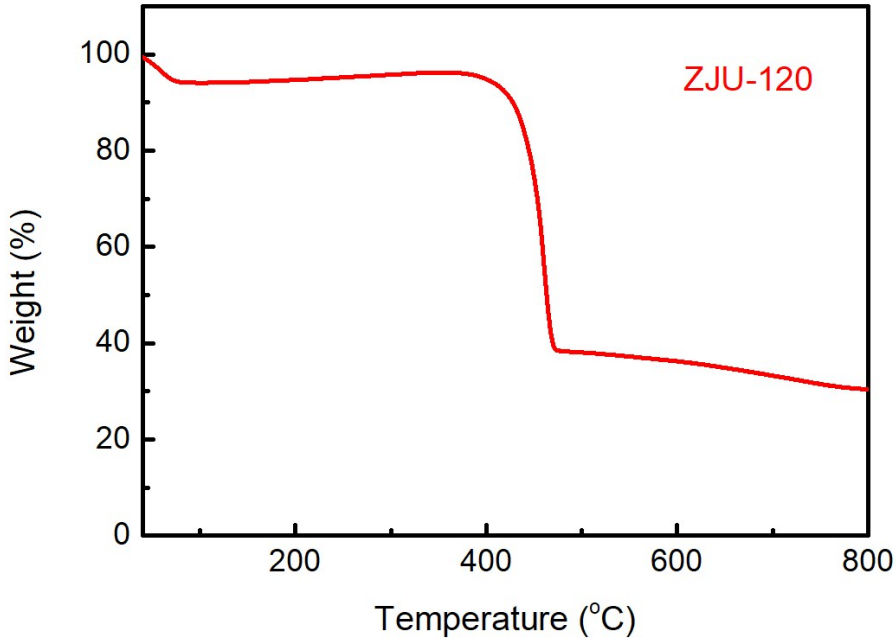

Figure S10. TGA curve of as-synthesized ZJU-120.

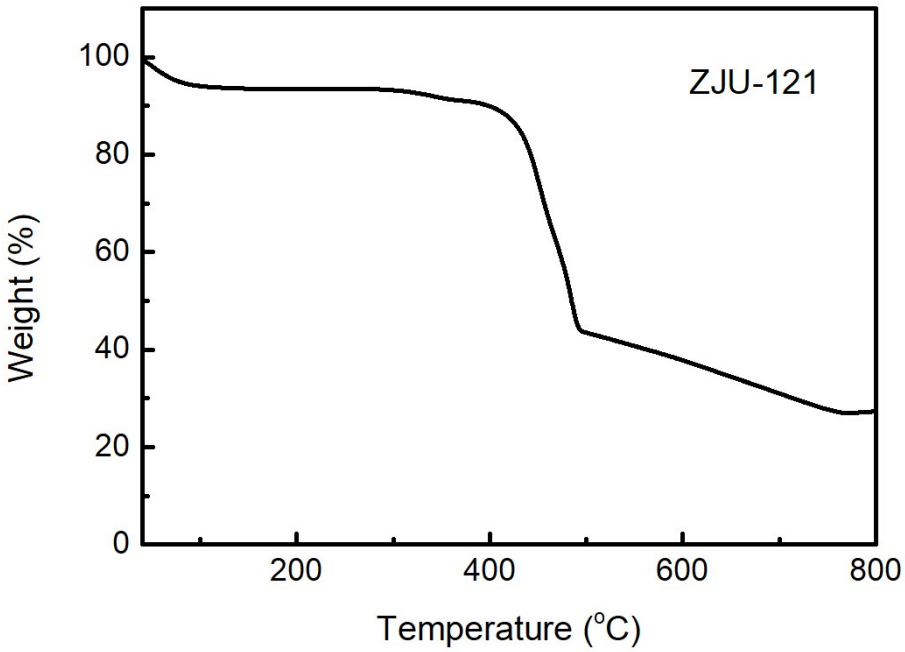

Figure S11. TGA curve of as-synthesized ZJU-121.

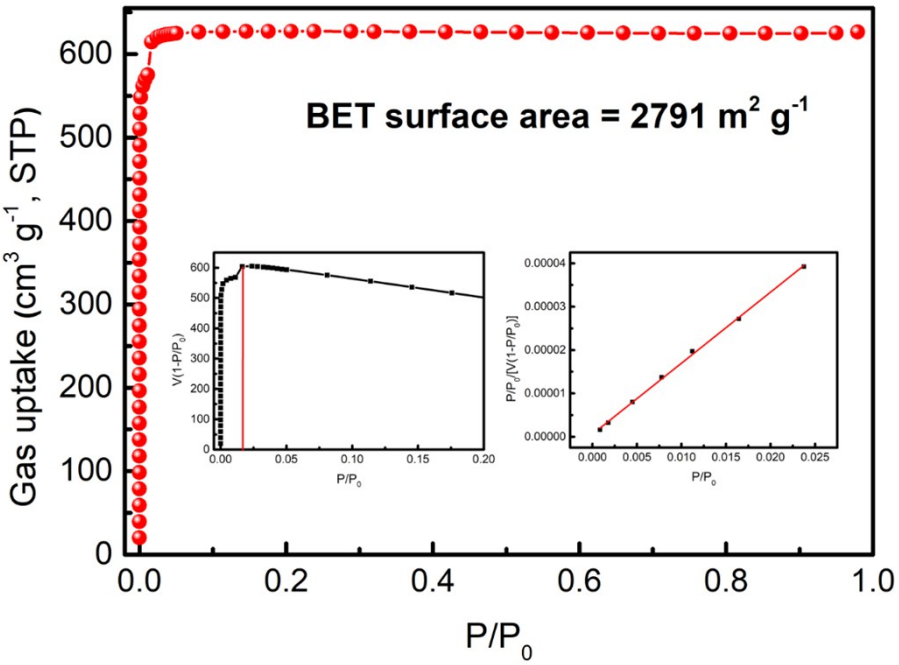

Figure S12. Nitrogen isotherm at 77 K with consistency and BET plots for the activated $Ni(bdc)(ted)_{0.5}$ sample.

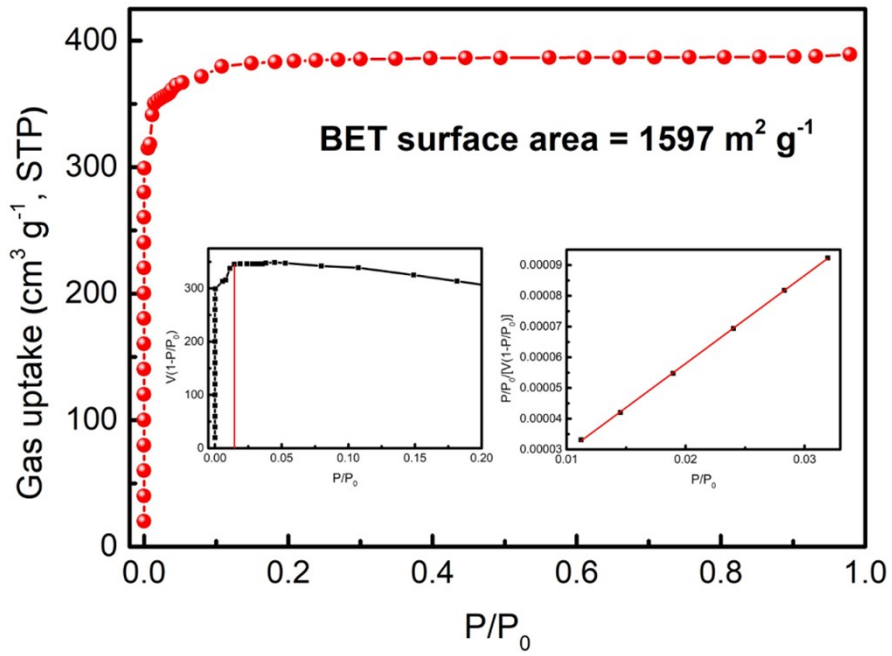

Figure S13. Nitrogen isotherm at 77 K with consistency and BET plots for the activated ZJU-120a sample.

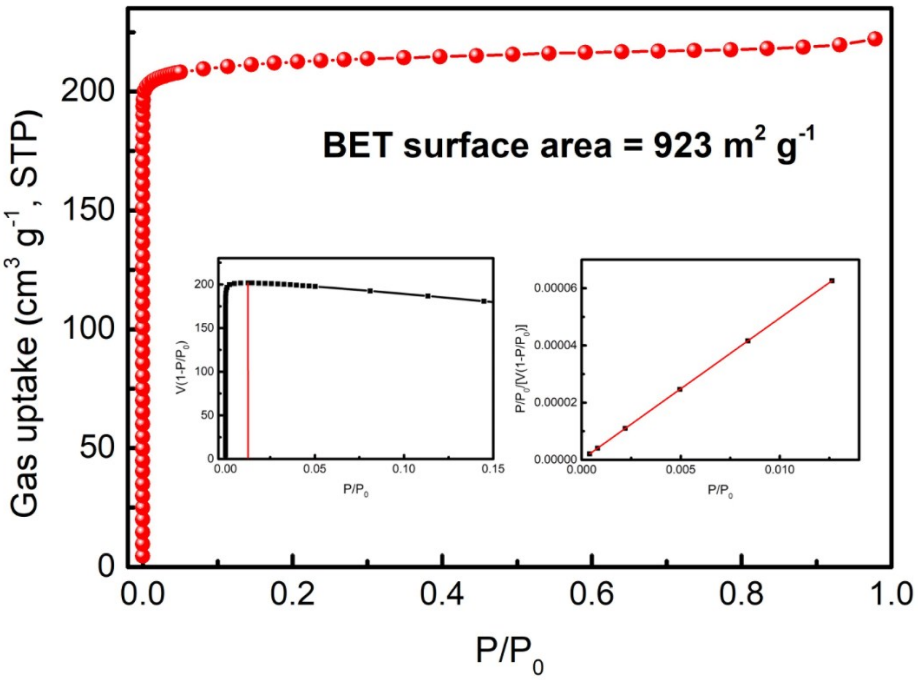

Figure S14. Nitrogen isotherm at 77 K with consistency and BET plots for the activated ZJU-121a sample.

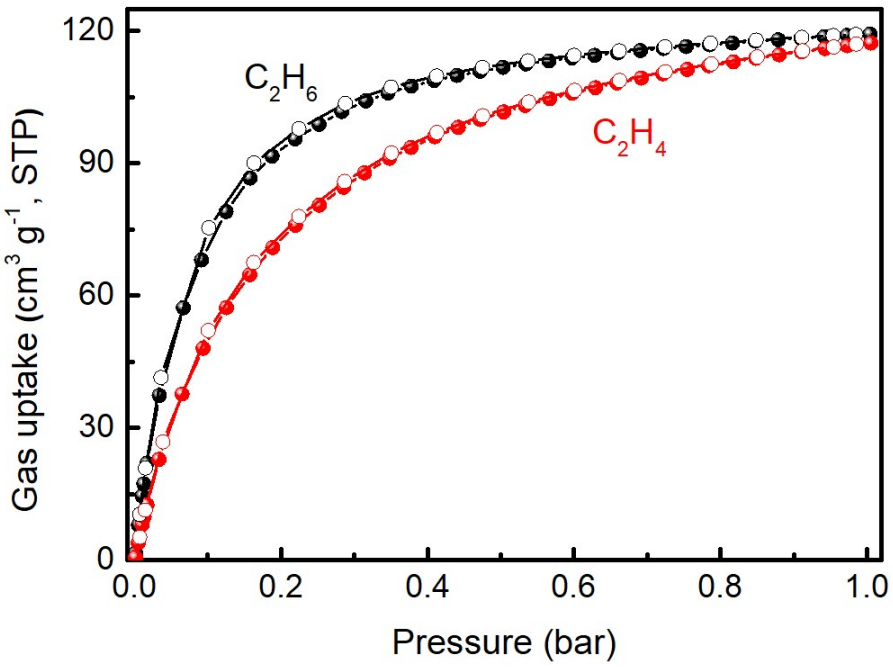

Figure S15. Adsorption isotherms of C_2H_6 (black) and C_2H_4 (red) for ZJU-120a at 273 K up to 1 bar.

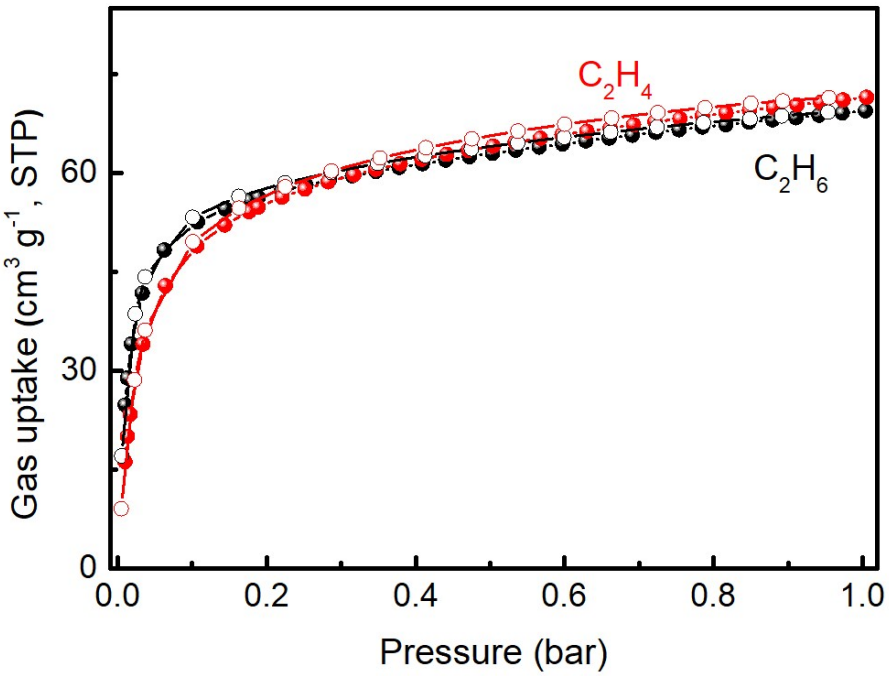

Figure S16. Adsorption isotherms of C_2H_6 (black) and C_2H_4 (red) for ZJU-121a at 296 K up to 1 bar.

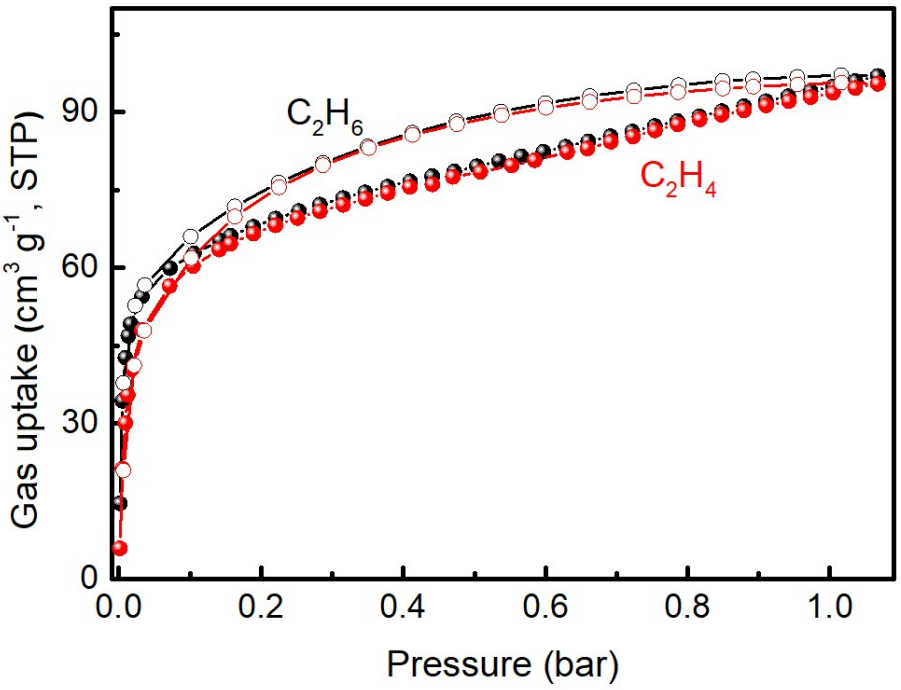

Figure S17. Adsorption isotherms of C_2H_6 (black) and C_2H_4 (red) for ZJU-121a at 273 K up to 1 bar.

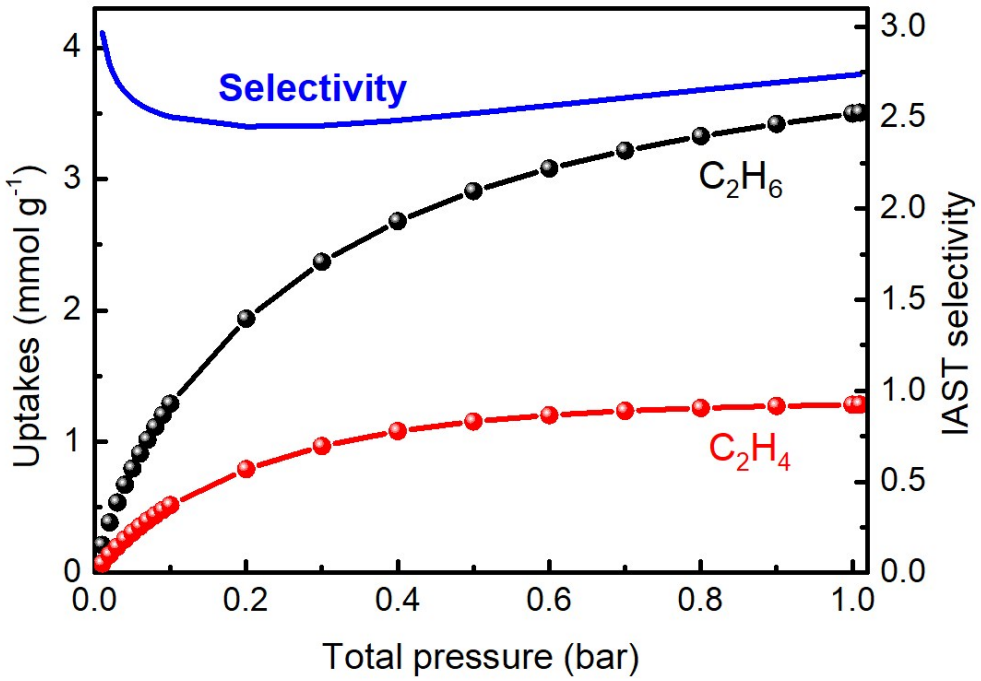

Figure S18. Predicted mixture adsorption isotherms and selectivity of ZJU-120a predicted by the IAST method for a 50/50 (v/v) C_2H_6/C_2H_4 mixture at 296 K.

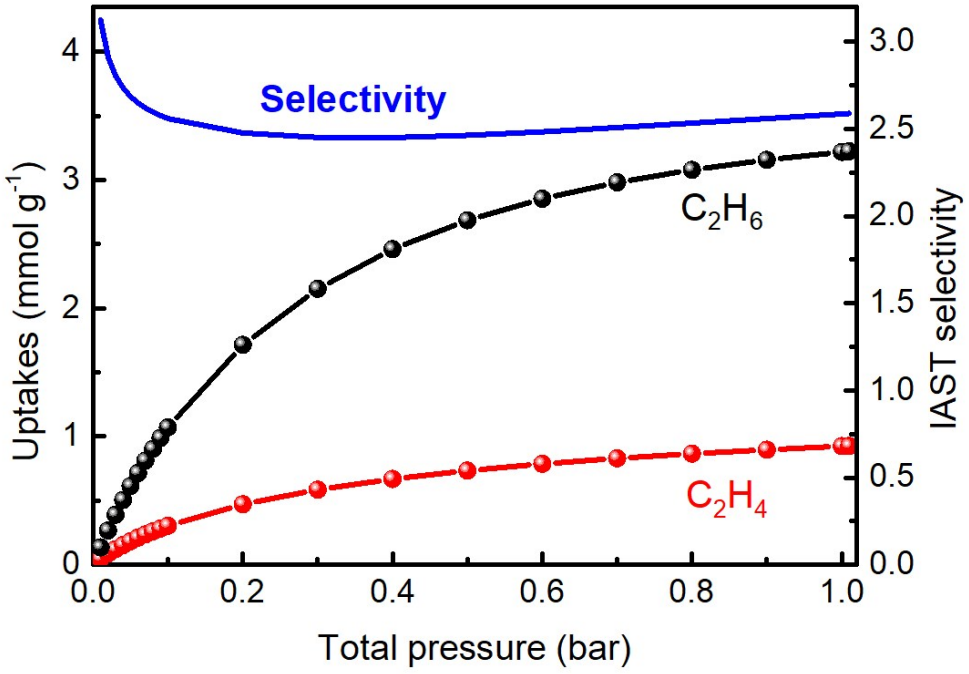

Figure S19. Predicted mixture adsorption isotherms and selectivity of ZJU-120a predicted by the IAST method for a 10/90 (v/v) C_2H_6/C_2H_4 mixture at 296 K.

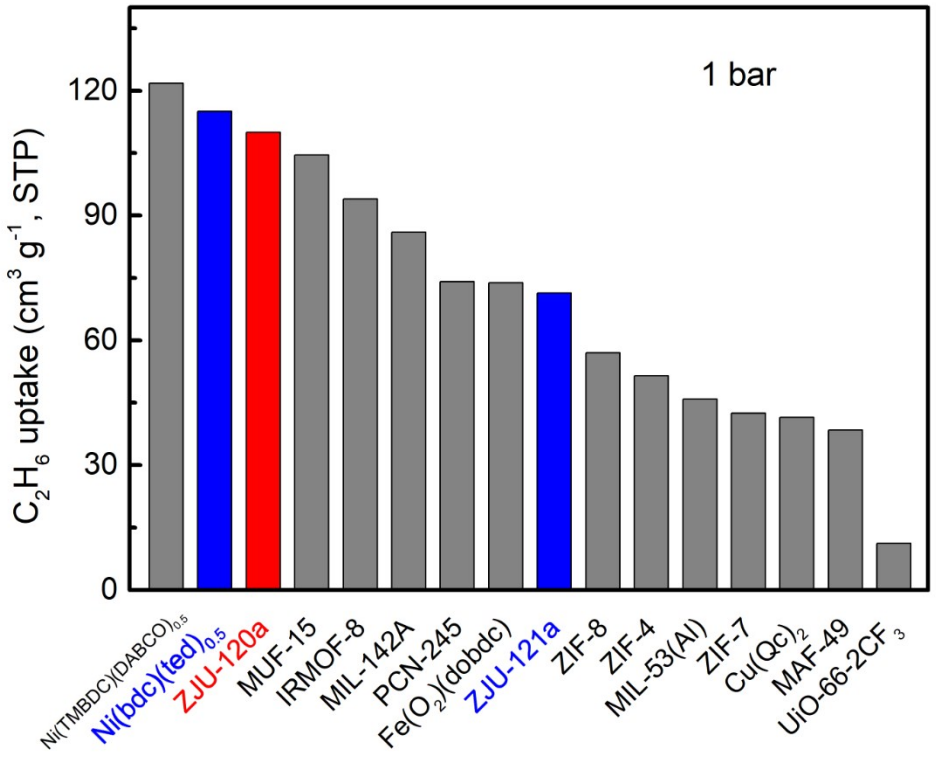

Figure S20. Comparison of C_2H_6 uptake for ZJU-120a and other best-performing materials at 1 bar.

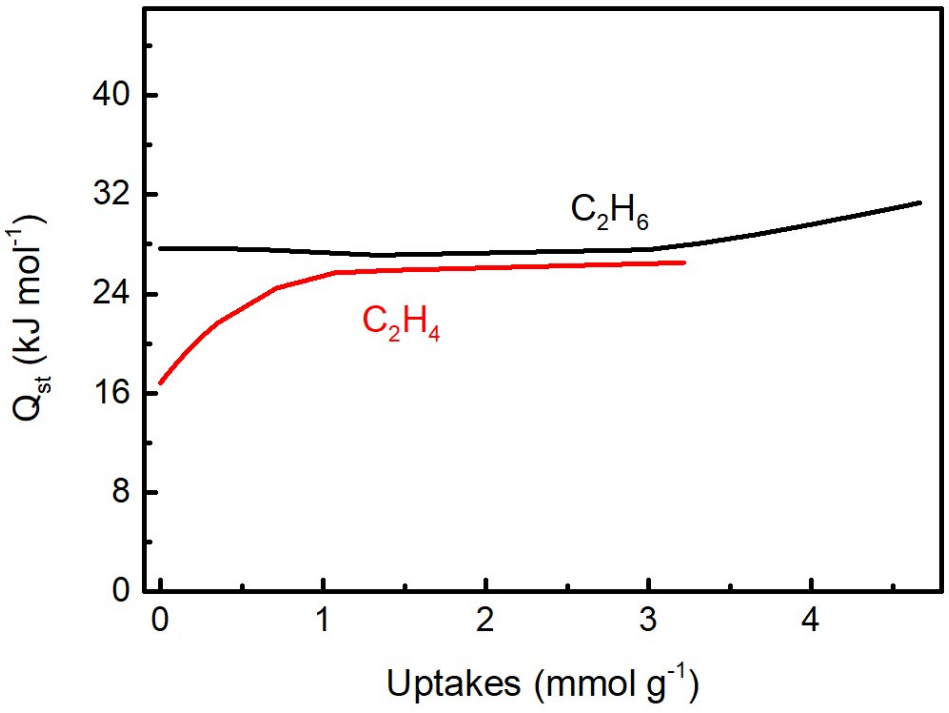

Figure S21. Heats of adsorption (Q_{st}) of C_2H_6 (black) and C_2H_4 (red) for ZJU-120a.

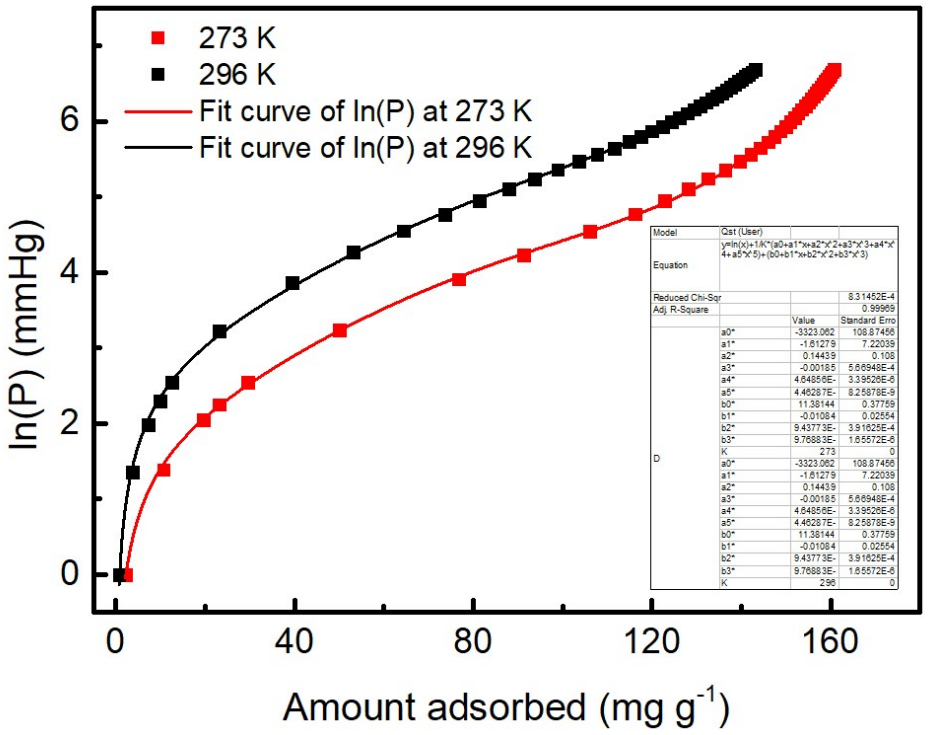

Figure S22. Virial fitting of the C_2H_6 adsorption isotherms for ZJU-120a.

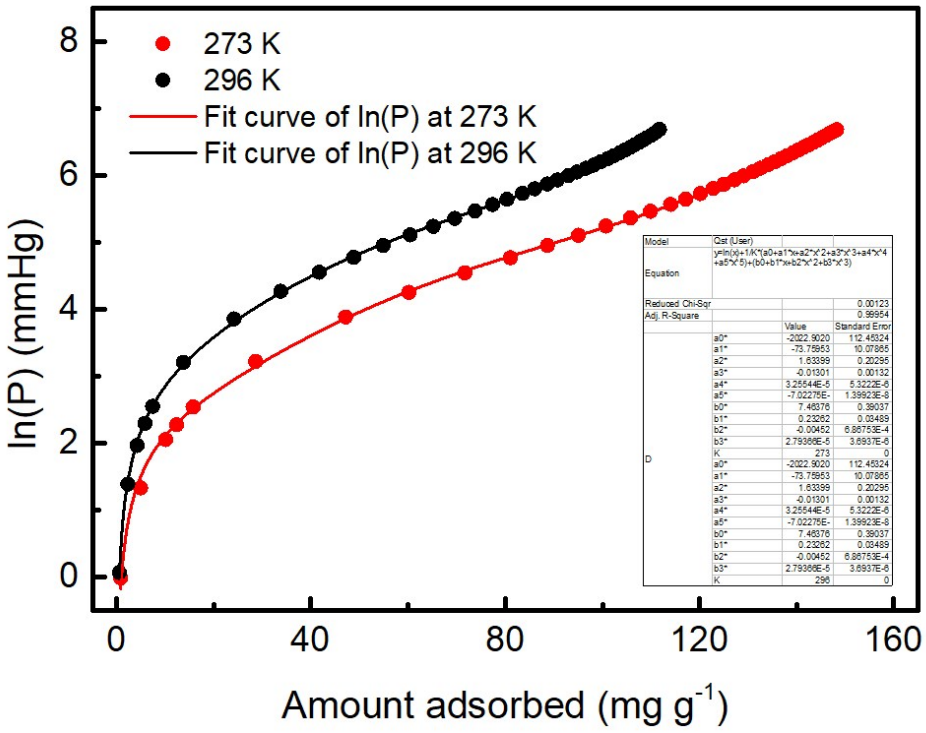

Model	Gst (User)		
Equation	y=ln(x)+1/K*(a0+a1*x+a2*x^2+a3*x^3+a4*x^4+a5*x^5)+(b0+b1*x+b2*x^2+b3*x^3)		
Reduced Chi-Sqr			0.00123
Adj. R-Square			0.99954
		Value	Standard Error
D	a0*	-2022.5020	112.45824
	a1*	-73.75953	10.07885
	a2*	1.63399	0.20295
	a3*	-0.01301	0.00132
	a4*	3.25544E-5	5.3222E-6
	a5*	-7.02275E-	1.39923E-8
	b0*	7.46376	0.39037
	b1*	0.23262	0.03489
	b2*	-0.00452	6.86753E-4
	b3*	2.79369E-5	3.6937E-6
	K	273	0
	a0*	-2022.5020	112.45824
	a1*	-73.75953	10.07885
	a2*	1.63399	0.20295
	a3*	-0.01301	0.00132
	a4*	3.25544E-5	5.3222E-6
	a5*	-7.02275E-	1.39923E-8
	b0*	7.46376	0.39037
	b1*	0.23262	0.03489
	b2*	-0.00452	6.86753E-4
	b3*	2.79369E-5	3.6937E-6
	K	296	0

Figure S23. Virial fitting of the C_2H_4 adsorption isotherms for ZJU-120a.

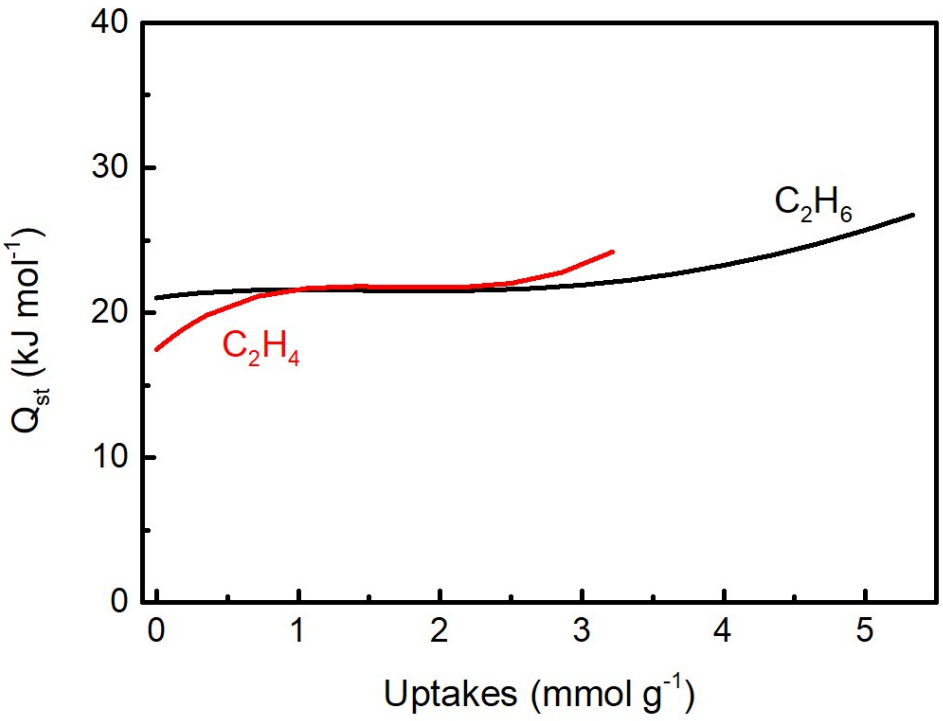

Figure S24. Heats of adsorption (Q_{st}) of C_2H_6 (black) and C_2H_4 (red) for $Ni(bdc)(ted)_{0.5}$.

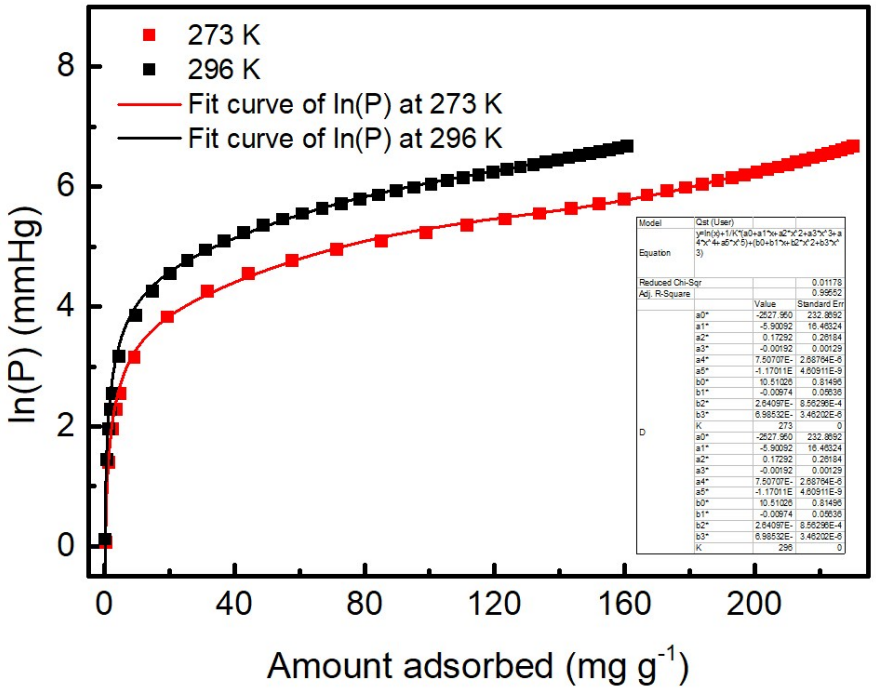

Figure S25. Virial fitting of the C_2H_6 adsorption isotherms for $Ni(bdc)(ted)_{0.5}$.

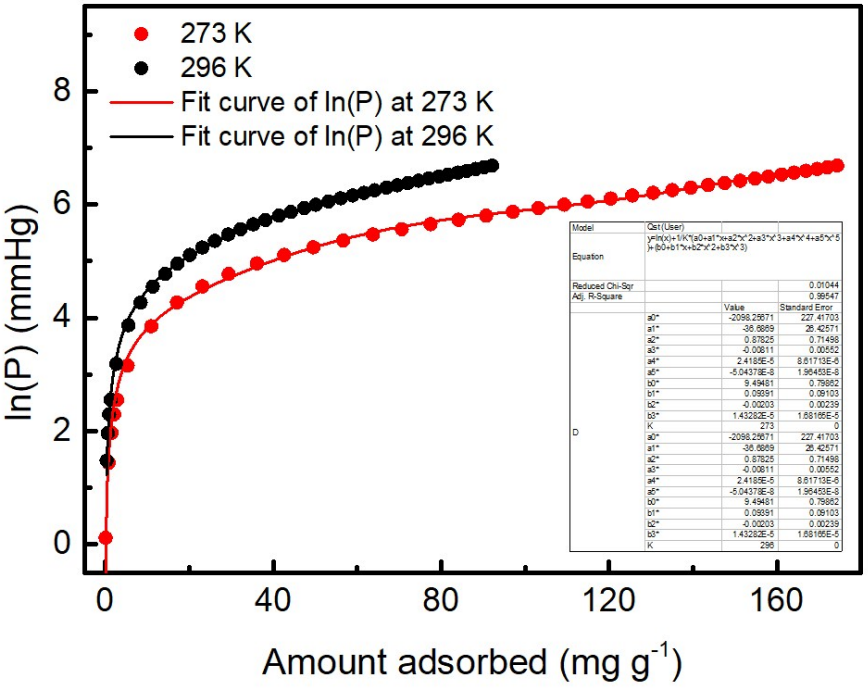

Figure S26. Virial fitting of the C_2H_4 adsorption isotherms for $Ni(bdc)(ted)_{0.5}$.

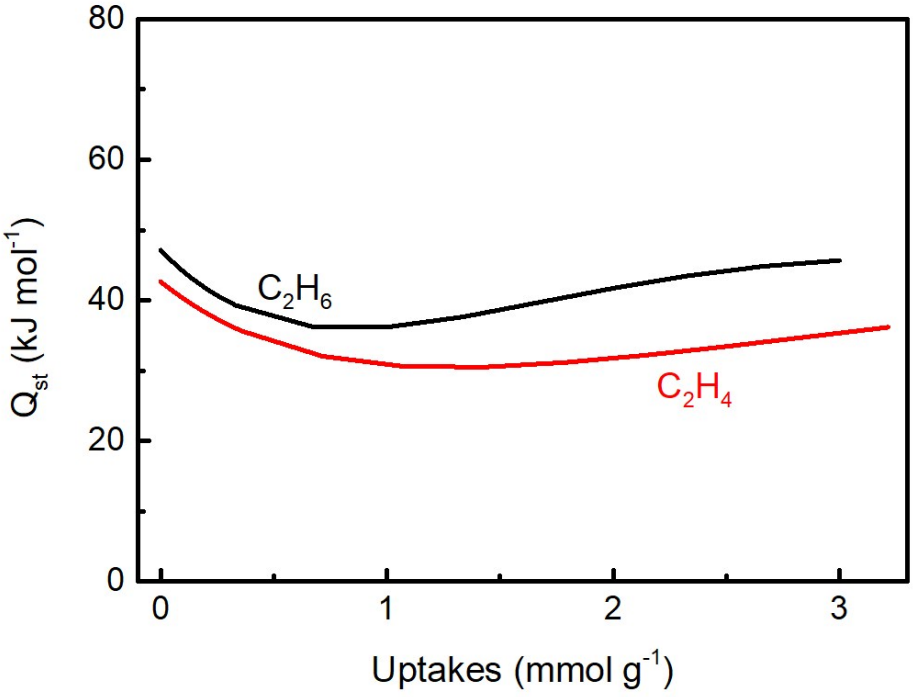

Figure S27. Heats of adsorption (Q_{st}) of C_2H_6 (black) and C_2H_4 (red) for ZJU-121a.

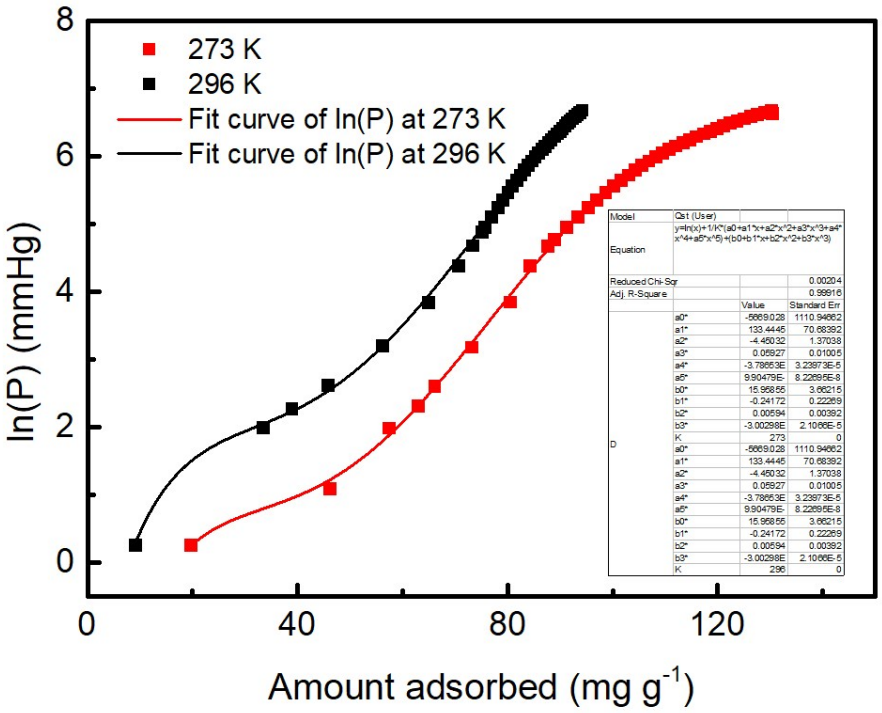

Figure S28. Virial fitting of the C_2H_6 adsorption isotherms for ZJU-121a.

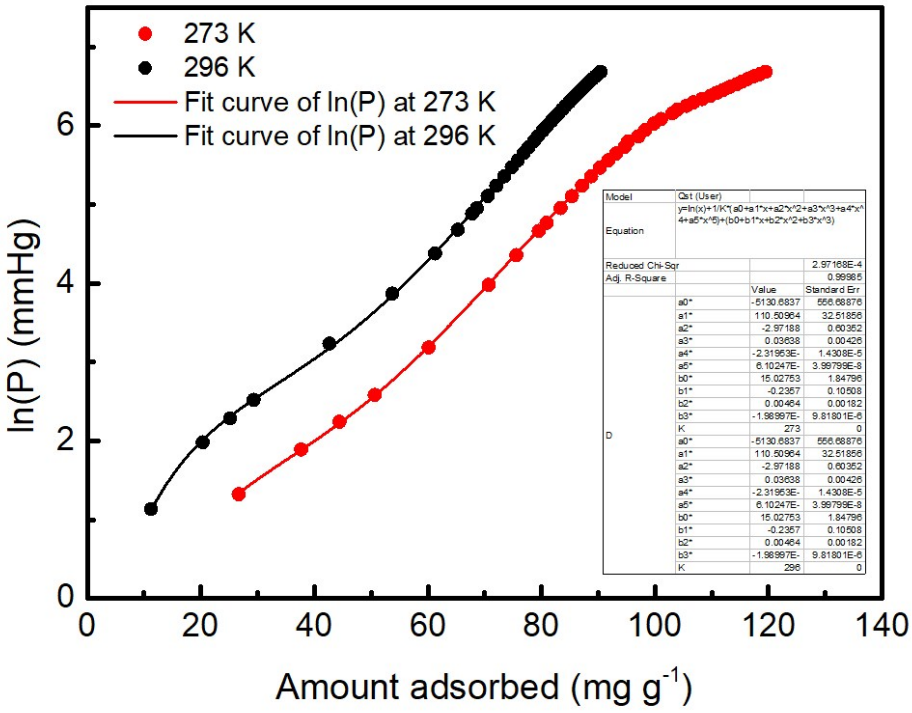

Figure S29. Virial fitting of the C_2H_4 adsorption isotherms for ZJU-121a.

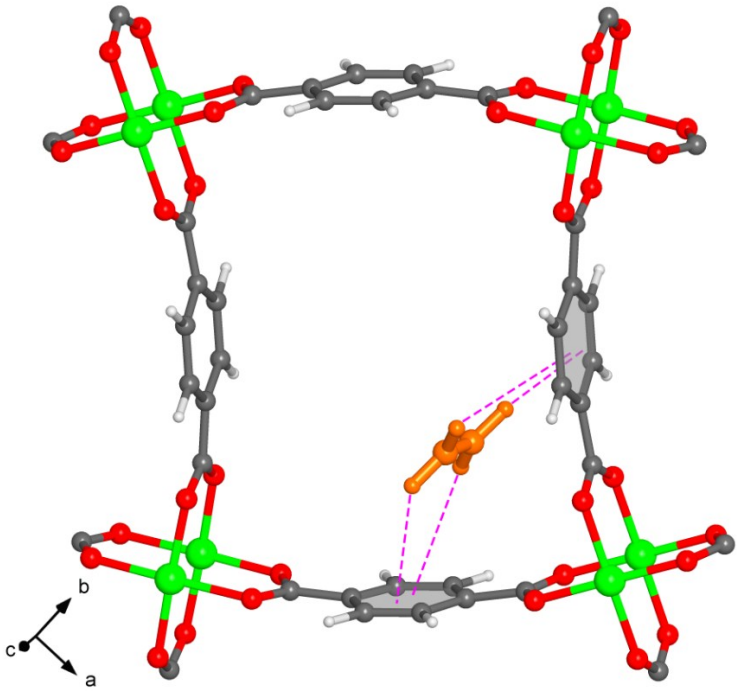

Figure S30. The optimal C_2H_4 adsorption site in Ni(bdc)(ted)$_{0.5}$ obtained from DFT-D calculations. Colour code: Ni (green), O (red), N (blue), C (grey), and H (white).

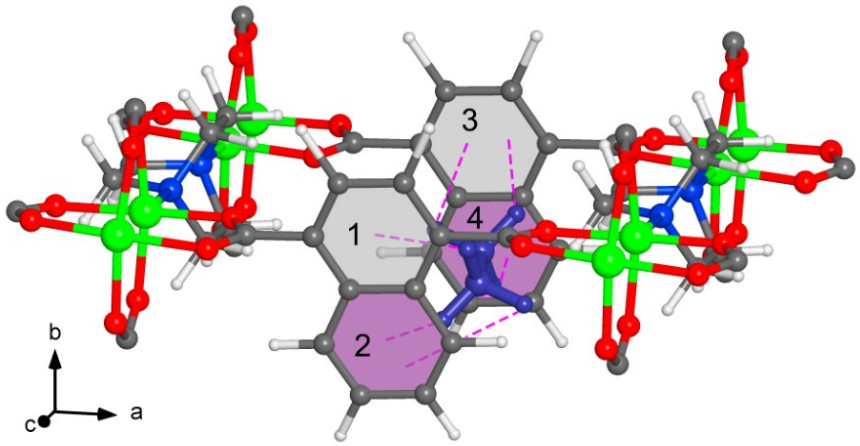

Figure S31. The optimal C_2H_6 adsorption site in ZJU-120a (along c axis) obtained from DFT-D calculations. Colour code: Ni (green), O (red), N (blue), C (grey), and H (white).

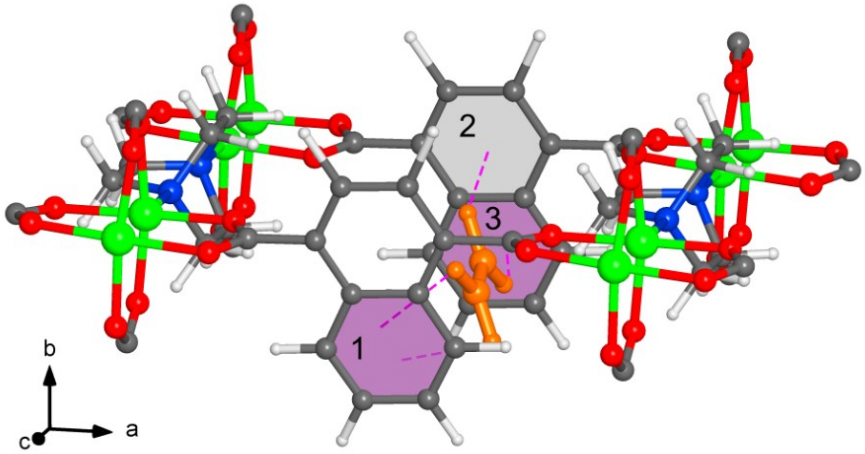

Figure S32. The optimal C_2H_4 adsorption site in ZJU-120a (along c axis) obtained from DFT-D calculations. Colour code: Ni (green), O (red), N (blue), C (grey), and H (white).

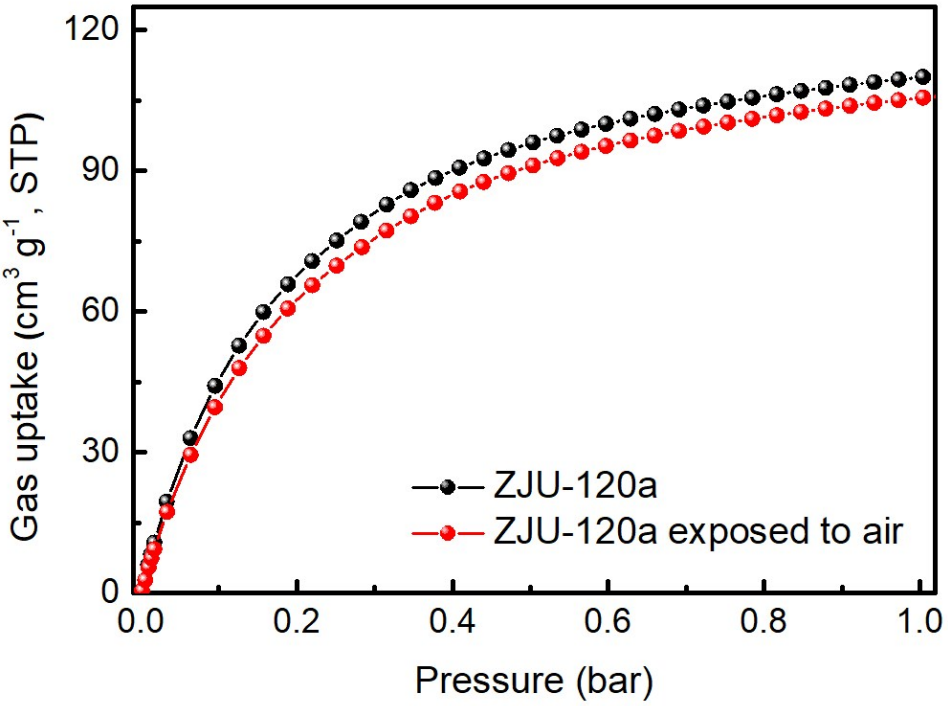

Figure S33. Comparison of C_2H_6 adsorption isotherms at 296 K of ZJU-120a (black) and the re-activated sample after the exposure to air (red) for one month, confirming its good chemical stability.

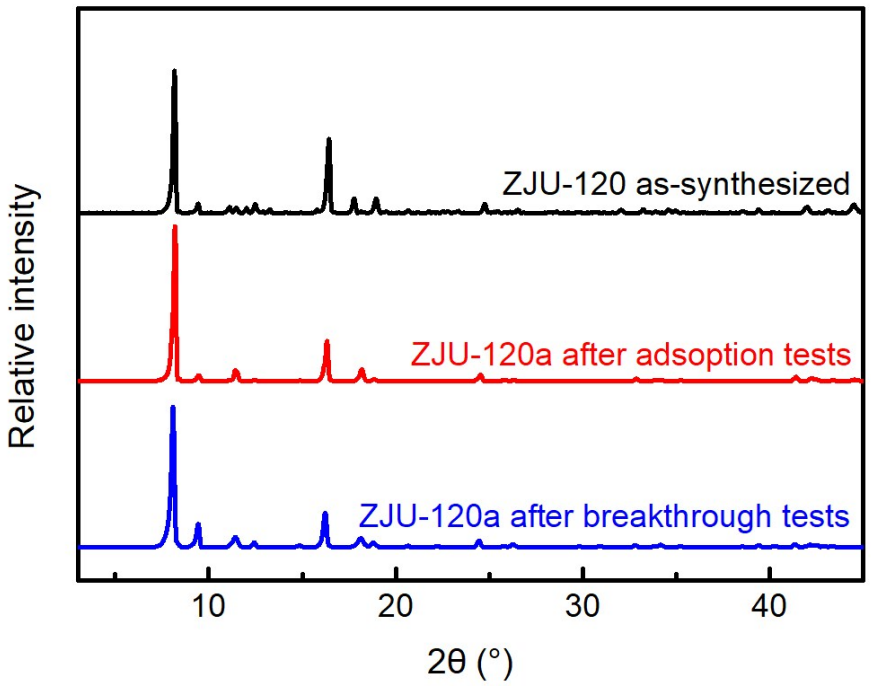

Figure S34. PXRD patterns of as-synthesized ZJU-120 (black) and the samples after adsorption tests (red) and breakthrough tests (blue).

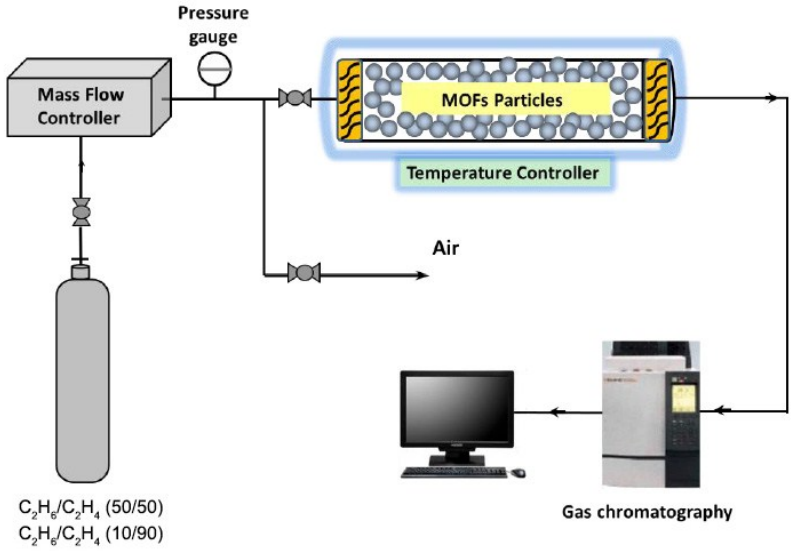

Figure S35. Schematic illustration of the apparatus for the breakthrough experiments.

References

1 W. Liang, F. Xu, X. Zhou, J. Xiao, Q. Xia, Y. Li and Z. Li, *Chem. Eng. Sci.*, 2016, **148**, 275.

2 L. Li, R.-B. Lin, R. Krishna, H. Li, S. Xiang, H. Wu, J. Li, W. Zhou and B. Chen, *Science*, 2018, **362**, 443.

3 R.-B. Lin, H. Wu, L. Li, X.-L. Tang, Z. Li, J. Gao, H. Cui, W. Zhou and B. Chen, *J. Am. Chem. Soc.*, 2018, **140**, 12940.

4 P.-Q. Liao, W.-X. Zhang, J.-P. Zhang and X.-M. Chen, *Nat. Commun.*, 2015, **6**, 8697.

5 J. Pires, J. Fernandes, K. Dedecker, J. R. Gomes, G. Perez-Sanchez, F. Nouar, C. Serre and M. L. Pinto, *ACS Appl. Mater. Inter.*, 2019, **11**, 27410.

6 M. Hartmann, U. Böhme, M. Hovestadt and C. Paula, *Langmuir.*, 2015, **31**, 12382.

7 X. Wang, Z. Niu, A. M. Al-Enizi, A. Nafady, Y. Wu, B. Aguila, G. Verma, L. Wojtas, Y.-S. Chen, Z. Li and S. Ma, *J. Mater. Chem. A*, 2019, **7**, 13585.

8 O. T. Qazvini, R. Babarao, Z.-L. Shi, Y.-B. Zhang and S. G. Telfer, *J. Am. Chem. Soc.*, 2019, **141**, 5014.

9 U. Böhme, B. Barth, C. Paula, A. Kuhnt, W. Schwieger, A. Mundstock, J. Caro and M. Hartmann, *Langmuir.*, 2013, **29**, 8592.

10 D. Lv, R. Shi, Y. Chen, Y. Wu, H. Wu, H. Xi, Q. Xia and Z. Li, *ACS Appl. Mater. Inter.*, 2018, **10**, 8366.

11 J. Pires, M. L. Pinto and V. K. Saini, *ACS Appl. Mater. Inter.*, 2014, **6**, 12093.

12 Y. Chen, H. Wu, D. Lv, R. Shi, Y. Chen, Q. Xia and Z. Li, *Ind. Eng. Chem. Res.*, 2018, **57**, 4063.

13 C. Gücüyener, J. van den Bergh, J. Gascon and F. Kapteijn, *J. Am. Chem. Soc.*, 2010, **132**, 17704.

14 R. P. Ribeiro, B. C. Camacho, A. Lyubchyk, I. A. Esteves, F. J. Cruz and J. P. Mota, *Micropor. Mesopor. Mat*, 2016, **230**, 154.